

From Weibel seeds to dynamo beyond pair-plasmas

Lise Hanebring¹†, James Juno², Ammar Hakim², Jason M. TenBarge²
and István Pusztai¹

¹Department of Physics, Chalmers University of Technology, Gothenburg 41296, Sweden

²Princeton Plasma Physics Laboratory, Princeton, New Jersey 08543, USA

(Received xx; revised xx; accepted xx)

Bridging the spatiotemporal scales of magnetic seed field generation and subsequent dynamo amplification in the weakly collisional intracluster medium presents an extreme numerical challenge. We perform collisionless turbulence simulations with initially unmagnetized electrons that capture both magnetic seed generation via the electron Weibel instability and the ensuing dynamo amplification. Going beyond existing pair-plasma studies, we use an ion-to-electron mass ratio of 100 for which we find electron and ion dynamics are sufficiently decoupled. These simulations are enabled by the 10-moment collisionless fluid solver of `Gkeyll`, which evolves the full pressure tensor for all species. The electron heat-flux closure regulates pressure isotropization and effectively sets the magnetic Reynolds number. We investigate how the strength of the closure influences the transition between a regime reminiscent of previous kinetic pair-plasma simulations and a more MHD-like dynamo regime.

1. Introduction

The magnetic fields permeating the universe (Carilli & Taylor 2002; Govoni & Feretti 2004; Brandenburg & Subramanian 2005; Kulsrud & Zweibel 2008; Brandenburg & Ntormousi 2023) profoundly affect the development of astrophysical systems from stellar to cosmological scales. They play important roles in the dynamics of astrophysical plasmas, through, e.g., setting the transport properties of the medium, such as the viscosity (Zhuravleva *et al.* 2019; Kunz *et al.* 2014) and heat conductivity (Roberg-Clark *et al.* 2016, 2018; Komarov *et al.* 2016, 2018), and by providing channels for bulk plasma heating and particle energization (Sironi *et al.* 2025; Guo *et al.* 2024; Amano *et al.* 2022; Matthews *et al.* 2020). While the origin of cosmic magnetic fields remains an open question, growing observational evidence based on Faraday rotation (Bonafede *et al.* 2010), synchrotron emission (Feretti *et al.* 2012), and Zeeman splitting (Crutcher 2012) indicates dynamically important magnetic fields in galaxies and galaxy clusters. This observational evidence is consistent with these fields being created and sustained through dynamo action. This inherently three-dimensional (3D) process that naturally arises in turbulent plasma environments is believed to have exponentially amplified seed magnetic fields to equipartition levels, where the magnetic energy content is comparable to the kinetic energy of the turbulent flows, on timescales shorter than the Hubble time.

More than a century after Joseph Larmor proposed the dynamo phenomenon to explain the solar magnetic field (Larmor 1919), the role of dynamo in producing stellar and planetary magnetic fields is well established through a magnetohydrodynamic (MHD) modeling of these strongly collisional systems (Käpylä *et al.* 2023; Schubert & Soderlund

† Email address for correspondence: liseha@chalmers.se

2011; Tobias 2021). The mean free path of Coulomb collisions in galaxies and the intracluster medium (ICM) of galaxy clusters, however, is typically larger than the relevant turbulent length-scales. Thus, the large-scale properties of these weakly collisional environments are governed by kinetic microphysics instead of Coulomb collisions. Even though a large body of research into the turbulent dynamo in such systems is based on MHD modeling (Schekochihin *et al.* 2004; Porter *et al.* 2015; Vazza *et al.* 2017; Korpi-Lagg *et al.* 2024), it has become clear that addressing the question with tools beyond MHD would be desirable (Rincon 2019). On the other hand, the multi-scale and inherently 3D nature of turbulent dynamo, which is difficult enough to model with MHD, now becomes an outstanding computational challenge.

A fully kinetic treatment of systems beyond unity mass-ratio of the plasma particle species remains computationally prohibitively expensive. Hybrid (kinetic ion, fluid electron) modeling established the importance of a rich microphysics (Rincon *et al.* 2016; St-Onge & Kunz 2018), where instabilities play a key role not only in setting the macroscopic transport properties of the plasma but also breaking adiabatic invariance, which would otherwise strictly inhibit dynamo action (Helander *et al.* 2016). This is an important aspect, since the intra-cluster medium is extremely well magnetized, with typical Larmor radii being of planetary size, compared to the megaparsec scale system size. Another issue is that most of the proposed seed generation mechanisms, such as the Biermann battery (Biermann 1950) at the ionization fronts of the early universe (Subramanian *et al.* 1994), yield tiny magnetic fields (typically $\sim 10^{-24}$ T) (Langer & Durrive 2018; Subramanian 2016; Durrive & Langer 2015). These fields are unable to magnetize the plasma, in which case the dynamo is significantly less efficient due to a kinetic damping of the magnetic field (Pusztai *et al.* 2020).

Recent fully kinetic studies in pair-plasmas offer a new paradigm where the electron Weibel instability (Weibel 1959), driven by pressure anisotropies naturally developing in collisionless turbulent plasmas, provides the seed for dynamo (Zhou *et al.* 2023; Pucci *et al.* 2021; Sironi *et al.* 2023). This instability saturates as the electrons start to get magnetized at the scale of the instability[†], corresponding to sizable seed fields ($\sim 10^{-14}$ T for typical ICM turbulence parameters). Numerical simulations that connect the Weibel seed generation and the dynamo processes are important to establish that fields at large scales, i.e., the outer scales of the turbulence, can also be generated from the Weibel seeds in a self-consistent manner, especially in the light of recent work by Liu *et al.* (2025) pointing out that such an inverse cascade could be suppressed by the firehose instability. In addition moving beyond pair-plasmas is desirable to explore the impact of the scale separations induced by the ion-electron mass-ratio.

In this paper we use the 10-moment solver of `Gkeyll`[‡] (Wang *et al.* 2015, 2020) to perform 3D simulations of forced turbulence at a mass-ratio where ion and electron processes are significantly decoupled, which incorporate both the electron Weibel instability and the dynamo phases of magnetic field generation. The 10-moment solver of `Gkeyll` evolves the full pressure tensor, thereby retaining relevant pressure anisotropy driven instabilities of high-beta plasmas, including the Weibel instability in the non-magnetized case. In addition, being implicit permits stepping over unimportant spatiotemporal scales, such as the Debye scale, allowing a larger flexibility in exploring various plasma parameter regimes. When the electron pressure isotropization by the heat flux closure is weak, our simulation results are qualitatively similar to previous kinetic simulations in pair plasmas,

[†] This saturation condition borne out of simulations of Califano *et al.* (1998) can provide a rough estimate, however at small pressure anisotropy relevant to our investigation, saturation occurs when the current in the Weibel filaments reach the *Alfvén current* (Kato 2005).

[‡] <https://github.com/amarhakim/gkeyll>

apart from electrons and ions playing separate roles here. When the electron pressure is more strongly driven towards isotropy, the results align better with expectations from magnetohydrodynamics.

The article is organized as follows: After describing the numerical model in Sec. 2.1, and defining effective Reynolds numbers in the absence of explicit viscosity and resistivity in Sec. 2.2, we describe the simulation settings in Sec. 2.3 and briefly comment on Weibel instabilities in our context in Sec. 2.4. The results of our baseline case are presented in Sec. 3.1, then we discuss a scan of electron pressure isotropization in Sec. 3.2. Finally we summarize and discuss our results in Sec. 4.

2. Methods

2.1. The 10-moment collisionless fluid system

Our simulations use the 10-moment collisionless fluid model of the **Gkeyll** continuum plasma physics solver framework. The 10-moment model employed here uses the following set of non-relativistic moment equations:

$$\frac{\partial n}{\partial t} + \frac{\partial}{\partial x_j} (n u_j) = 0, \quad (2.1)$$

$$mn \frac{\partial u_j}{\partial t} + m n u_k \frac{\partial u_j}{\partial x_k} + \frac{\partial p_{jk}}{\partial x_k} = n q [E_j + \epsilon_{jkl} u_k B_l], \quad (2.2)$$

$$\frac{\partial p_{jk}}{\partial t} + \frac{\partial}{\partial x_l} (p_{jk} u_l) + p_{jl} \frac{\partial u_k}{\partial x_l} + p_{kl} \frac{\partial u_j}{\partial x_l} + \frac{\partial q_{jkl}}{\partial x_l} = \frac{q}{m} [\epsilon_{jlm} p_{lk} B_m + \epsilon_{klm} p_{lj} B_m], \quad (2.3)$$

where we have suppressed the species index α with mass and charge m_α and q_α , but otherwise $n_\alpha = \int f_\alpha d^3 v$ is the density, where $f_\alpha(\mathbf{x}, \mathbf{v}, t)$ is the particle distribution function, and the fluid flow velocity vector, pressure tensor, and heat flux tensor components are defined by $u_{j,\alpha} = n_\alpha^{-1} \int v_j f_\alpha d^3 v$, $p_{jk,\alpha} = m_\alpha \int (v_j - u_j)(v_k - u_k) f_\alpha d^3 v$, and $q_{jkl,\alpha} = m_\alpha \int (v_j - u_j)(v_k - u_k)(v_l - u_l) f_\alpha d^3 v$, respectively. Furthermore E_j and B_j denote the electric and magnetic field components, which are evolved according to Maxwell's equations, $\partial_t \mathbf{B} = -\nabla \times \mathbf{E}$ and $\partial_t \mathbf{E} = c^2 \nabla \times \mathbf{B} - \epsilon_0^{-1} \sum_\alpha q_\alpha n_\alpha \mathbf{u}_\alpha$. The solver uses a locally implicit scheme for the source terms, while solving the homogeneous portion of the equations by the wave propagation method (LeVeque 1997). This approach allows certain unimportant scales to be under-resolved without leading to numerical difficulties. In particular, our simulations strongly under-resolve the Debye scale, which would not be possible in most particle-in-cell kinetic codes. This provides us greater flexibility in the plasma parameter regimes considered.

Importantly, the full pressure tensor is evolved for each species, which allows some pressure anisotropy driven instabilities (Gary 1993) to be retained, such as the firehose instability (Walters *et al.* 2024), and with particular relevance to the current work, the Weibel instability. Previous work by Kuldinow & Hara (2025) employing the 10-moment system with a zero heat flux closure ($q_{jkl} = 0$) demonstrated that the model can predict electron Weibel instability growth rates in the long wavelength and the strongly driven limits and accurately reproduces the high wavenumber cutoff, as well as the nonlinear saturation level, of the instability.

Here, we use a closure that drives the system towards an isotropic pressure (Wang *et al.* 2015)

$$\frac{\partial q_{jkl,\alpha}}{\partial x_l} = k_{0,\alpha} \frac{v_{\text{th},\alpha}}{\sqrt{2}} (p_{jk,\alpha} - p_\alpha \delta_{jk}), \quad (2.4)$$

where $p_\alpha = \delta_{jk} p_{jk,\alpha} / 3$ is the scalar pressure and $v_{\text{th},\alpha} = \sqrt{2 p_\alpha / (n_\alpha m_\alpha)}$ is the thermal

speed. The parameters $k_{0,\alpha}$ adjust the strength of the isotropization for each species. While other closures for the heat flux are available in `Gkeyll`, such as nonlocal (Ng *et al.* 2017) or gradient-based (Ng *et al.* 2020), we choose the local relaxation closure for its explicit connection to dissipation and our ability to determine effective Reynolds numbers from the choice of the closure parameter.

2.2. Effective Reynolds numbers

Unlike in resistive-MHD, where the concepts of dynamo theory have mostly been developed, in the 10-moment system, or a collisionless kinetic system for that matter, there is no explicit kinematic viscosity ν and magnetic diffusivity η . In addition, the corresponding damping rates of flow and magnetic perturbations can in general have different wavenumber (k) dependence to the $\propto k^2$ diffusive behavior. Thus the usual definitions of the fluid and magnetic Reynolds numbers, $\text{Re} = u_0 L / \nu$ and $\text{Rm} = u_0 L / \eta$, respectively, are less trivial to evaluate[†], and they have different implications concerning the scale separation between the outer scale and the fluctuation cutoff scales.

To put our results in context, it is nevertheless useful to quantify the magnetic and fluid damping in terms of analogous dimensionless quantities, comparing inverse timescales of processes creating and dissipating magnetic and fluid kinetic energy on the outer scale L . The fluid Reynolds number compares inertial processes $\sim u_0 / L$ to (viscous) flow damping $\sim \nu / L^2$, while the magnetic Reynolds number compares field line stretching by the flow $\sim u_0 / L$ to resistive dissipation of magnetic fields $\sim \eta / L^2$. Thus, a plausible generalization of these quantities is

$$\text{Re} = \frac{u_0 / L}{\gamma_U|_{k_0}} \quad \text{and} \quad \text{Rm} = \frac{u_0 / L}{\gamma_B|_{k_0}}, \quad (2.5)$$

where $\gamma_U|_{k_0}$ and $\gamma_B|_{k_0}$ are the damping rates of the mass flow and the magnetic field, respectively, taken at the wavenumber corresponding to the box scale $k = k_0 \equiv 2\pi / L$.

In Appendix A we confirm that the damping of the mass flow is governed by the ion closure parameter $k_{0,i}$, and the magnetic field damping by the electron closure parameter $k_{0,e}$. Such separation of the electron and ion physics requires the mass ratio to be sufficiently large. Specifically, the damping rate of the mass flow scales approximately as $\gamma_U \propto k^2 / k_{0,i}$, that is, with the same k -dependence as the diffusive flow damping in a viscous fluid. However, the damping rate of the magnetic field scales approximately as $\gamma_B \propto k^4 / k_{0,e}$, which is consistent with a hyperdiffusive damping.

Since the $k_{0,\alpha} \rightarrow 0$ limit of the 10-moment system is not singular, at sufficiently low values of the closure parameters $k_{0,\alpha}$ these scalings must be broken, and the damping rates saturate towards constant values. We are in the vicinity of such a saturation concerning $\gamma_B(k_{0,e})$ at our baseline parameters (to be detailed in the next section), however the scan in $k_{0,e}$ we will perform moves into the $\gamma_B \propto k_{0,e}^{-1}$ regime. Concerning the mass flows, we work in the $\gamma_U \propto k^2 / k_{0,i}$ regime, and we keep $k_{0,i}$ fixed.

2.3. Simulation settings

To be relevant to the fast turbulent dynamo in collisionless astrophysical media, our simulations must have sustained three-dimensional flows. In reality the flows are the result of gravitational collapse in the presence of dark matter, while our simulations include forced flows of non-gravitating baryonic matter in the plasma state. To produce fast dynamo at a relatively low value of the critical magnetic Reynolds number, we

[†] In particle based modeling, the effective collisionality may be calculated based on the statistics of pitch angle scattering caused by collective fields (Zhou *et al.* 2023).

drive our flows towards a simulation box-scale (L) Galloway-Proctor (GP) model flow (Galloway & Proctor 1992). More specifically, both the electrons and ions are accelerated by the same spatio-temporally varying acceleration $\mathbf{a}_\alpha(\mathbf{x}, t) = C_f \mathbf{U}_{\text{GP}}(\mathbf{x}, t)/t_{\text{str},i}$, which is proportional to the GP flow

$$\mathbf{U}_{\text{GP}}(\mathbf{x}, t) = u_0 \begin{bmatrix} A \sin(k_0 z + \sin \omega t) + C \cos(k_0 y + \cos \omega t) \\ A \cos(k_0 z + \sin \omega t) \\ C \sin(k_0 y + \cos \omega t) \end{bmatrix}, \quad (2.6)$$

where $t_{\text{str},i} = L/v_{\text{th},i}$ is the ion streaming time, u_0 is the nominal flow speed, $k_0 = 2\pi/L$ is the lowest wavenumber fitting the simulation box, the constants A and C determining the stirring geometry are chosen to be unity here, while the constant C_f sets the drive strength. In our baseline case, the representative flow speed is sub-sonic $u_0 = 0.35c_s$, with the sound speed $c_s = \sqrt{T_e/m_i}$, which defines the outer turnover time $t_{\text{turn}} = L/u_0$. As this is expected to be the characteristic timescale of dynamo growth, we use t_{turn} for time normalization with the nominal flow speed u_0 , while noting that the root mean square flow speed varies over time and is in general different from u_0 . We also set the stirring frequency of the flow to $\omega = 2\pi/t_{\text{turn}}$.

The simulations use a mass ratio of $m_i/m_e = 100$, and our baseline driving strength of $C_f = 2$ and $k_{0,i} = 13.6k_0$ are chosen such that the flows remain subsonic throughout the simulation. As a reference, this value of $k_{0,i}$ corresponds to $\text{Re} = 0.535$, while $k_{0,e} = 1k_0$ corresponds to $\text{Rm} = 307$, according to numerical damping rate tests like those presented in Appendix A, yielding a large magnetic Prandtl number $\text{Pm} = \text{Rm}/\text{Re} = 574$, which is relevant for the ICM.

Unlike particle-in-cell simulations, the continuum solvers of **Gkeyll** are essentially noise-free, thus we need to prescribe magnetic perturbations from which the Weibel instability can grow. Note that due to the rapid growth of this instability, the fact that we need such a seed magnetic field is not an issue, as in astrophysical settings the instability would produce macroscopic field strengths from arbitrarily small fluctuations on timescales shorter than those of the dynamo growth. Thus, as an initial condition we prescribe a magnetic field of the form

$$B_i(t = 0) = B_0 \sum_{j \neq i, n} b_{ij,n} \cos[nk_0(x_j + L\phi_{ij,n})], \quad (2.7)$$

with random relative amplitudes $b_{ij,n}$ and phases $\phi_{ij,n}$, both uniform on the unit interval, and a characteristic magnetic field strength B_0 . For our initial nominal field $B = B_0$, the thermal electron Larmor radius $\rho_e = v_{\text{th},e}m_e/(eB)$ is $\rho_e = 4.4L$, thus the system is non-magnetized. The system is non-relativistic, since $v_{\text{th},e}/c = 0.0625$.

A current consistent with this field, $\mathbf{j} = \mu_0^{-1} \nabla \times \mathbf{B}$, fully carried by the electrons, is also prescribed. In addition there is an initial flow velocity, equal for the electrons and the ions, given by Eq. (2.6) for $t = 0$. The initial ratio of the box-integrated magnetic energy and kinetic energy in the flows is 3.7×10^{-6} . With the inertial length, $\delta_\alpha = c/\omega_{p\alpha}$, and the plasma frequency $\omega_{p\alpha} = \sqrt{n_\alpha e_\alpha^2/(\epsilon_0 m_\alpha)}$ of species α , our baseline box size is $L = 70\delta_i$ in each direction. With a spatial resolution of $N = 140$ in each direction, such that the linear size of the finite volume is $\Delta x = L/140$, the ion inertial length is barely resolved $\delta_i = 2\Delta x$, while the electron inertial length is under-resolved $\delta_e = 0.2\Delta x$, along with the Debye length $\lambda_D \equiv \sqrt{\epsilon_0 T_e/(n_e e^2)} \approx 0.009\Delta x$. These scales are not a concern since the Debye scale is not playing an important role in the physics of the system, and the characteristic scales of the electron Weibel instability are significantly larger than δ_e due to the weak pressure anisotropy that develops in the system.

We finally note that our simulations are performed in SI units with physical parameters

comparable to those in (Pusztai *et al.* 2020). Namely, all physical constants have their actual value, except the ion mass that is $m_i = 100m_e$; both species have initially the same scalar temperature $T_e = T_i = 1$ keV, the electron density is $n_e = 2.3 \times 10^{28} \text{ m}^{-3}$, along with $k_0 = 2.58 \times 10^5 \text{ m}^{-1}$. Furthermore $B_0 = 1$ T. As the system has the scale invariance of a collisionless kinetic system, the fact that the plasma parameters (particularly the density) are not representative of the ICM is of no concern; we will present our results with practical normalizations.

2.4. The electron Weibel instability in non-magnetized collisionless plasma turbulence

The Weibel instability is a non-magnetized kinetic plasma instability that arises in the presence of an anisotropic velocity distribution. Transverse perturbations in the magnetic field deflect particles in a way that produces currents reinforcing the perturbation. As a result, it tends to generate filamentary current and magnetic field structures and acts to restore pressure isotropy. It plays important roles in astrophysical and laboratory plasmas (e.g. collisionless shocks, gamma-ray bursts, laser-plasma experiments) by generating sizable magnetic fields in initially non-magnetized or weakly magnetized environments, thereby qualitatively affecting particle dynamics. The instability has both electron and ion variants and additionally arises in pair-plasmas.

A large body of the Weibel literature is concerned with interpenetrating (often supersonic and relativistic) flow scenarios, due to its relevance for collisionless astrophysical shocks (Spitkovsky 2007; Kato & Takabe 2008; Medvedev *et al.* 2006; Medvedev & Loeb 1999), such as supernova remnants, and laser-plasma experiments (Huntington *et al.* 2015; Schoeffler *et al.* 2014). Pressure anisotropies appearing in such scenarios are typically substantial. However, as demonstrated by Zhou *et al.* (2022), the Weibel instability also naturally occurs in non-magnetized collisionless plasma turbulence, since phase mixing in sheared flows creates pressure anisotropy Δ_α . For subsonic turbulence, as relevant for our topic, this anisotropy is small.

The intuitive and conventional definition $\Delta_\alpha = p_{\parallel\alpha}/p_{\perp\alpha} - 1$ implicitly assumes a pressure tensor with diagonal components $\{p_{\parallel\alpha}, p_{\perp\alpha}, p_{\perp\alpha}\}$; this definition will need to be revised, since the pressure tensor in a non-magnetized system is non-gyrotropic, and has in general three unique eigenvalues. Thus, following Zhou *et al.* (2022), we use the definition $\Delta_\alpha = \sqrt{\langle (p_{\max,\alpha}/p_{\min,\alpha})^2 \rangle} - 1$, where $p_{\max,\alpha}$ is the highest eigenvalue of the pressure tensor, $p_{\min,\alpha}$ is the average of the two lower eigenvalues, and the angle bracket denotes the spatial (box) average.

Since the pressure anisotropies of ions and electrons that develop in the sheared flow tend to be comparable, the *electron* Weibel instability will dominate the magnetic field growth as it has higher growth rates than the ion mode. Specifically, in terms of the above anisotropy measure that is positive by construction, the fastest growing electron Weibel mode has a characteristic wavenumber $k \sim \Delta_e^{1/2}/\delta_e$ and a growth rate of $\gamma_B \sim \Delta_e^{3/2} \omega_{pe} v_{th,e}/c$. $\Delta_e < 1$ shifts the characteristic wavenumber to scales larger than the electron inertial length.

3. Results

3.1. Baseline case

First, we consider results for our baseline case with parameters given in Sec. 2.3, to establish the qualitative features of a representative simulation, before we consider the effect of the electron closure parameter and the box size in the following subsections.

The total magnetic field energy evolution is clearly separated into three phases, as

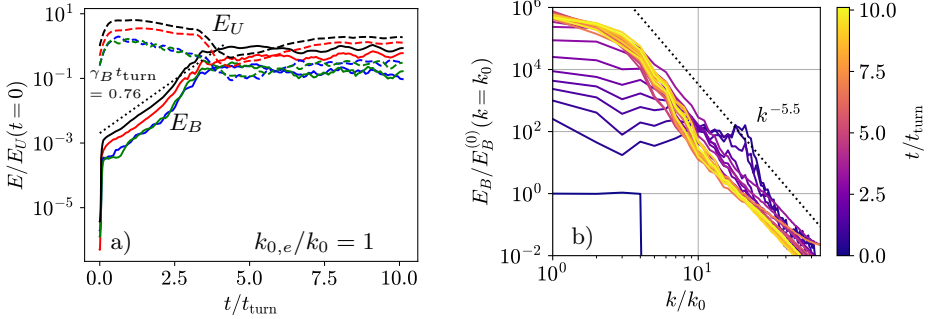


FIGURE 1. Magnetic field generation in the simulation with the baseline parameters. a) Time evolution of the box-integrated magnetic energy E_B (solid black curve) and kinetic energy in the flows E_U (dashed black), normalized to the initial value of E_U . With similar line styles, contributions from the $\{x, y, z\}$ components of \mathbf{U} and \mathbf{B} are shown in red, blue and green, respectively. The dotted line corresponds to an exponential growth of the magnetic field with a growth rate of $\gamma_B t_{\text{turn}} = 0.76$. b) Wave number spectra of the magnetic field energy. The wave number k is normalized to k_0 , and the spectrum is normalized to its value at $k = k_0$ for $t = 0$. For reference, the dotted line indicates a power law $k^{-5.5}$.

shown in Fig. 1a (solid black line, E_B). The first, very short phase, $t/t_{\text{turn}} < 0.1$, characterized by a very rapid magnetic field growth, is dominated by the electron Weibel instability. This phase is followed by a nearly exponential growth with a growth rate comparable to the outer turnover time, approximately $\gamma_B t_{\text{turn}} = 0.76$, as indicated by the dotted line, which abruptly saturates around $t/t_{\text{turn}} = 3.4$. As the magnetic energy approaches the kinetic energy in the flow E_U (dashed black line), the magnetic field brakes the flow and the flow energy drops, until eventually the two forms of energy establish near equipartition. It is noteworthy that the dynamo growth rate appears to increase towards the end of the growth phase even though the flow energy slowly decreases in time. This behavior could be caused by the increasing magnetization of the plasma leading to a reduced kinetic magnetic field damping.

The qualitative behavior is quite similar to that observed in kinetic simulations of pair-plasma dynamos by Zhou *et al.* (2023), such as the case shown in their Fig. 1a. Besides observing the same main phases of the magnetic field evolution, we also find that, in spite of the steady forcing of the flow, the flow energy decreases after a time comparable with t_{turn} , before it finds its long time quasi-equilibrium value. However, in the results here, as a consequence of driving a flow towards the GP model flow instead of a random flow drive, the contribution of the x -component of the flow to the kinetic energy is larger than that of the other directions, as seen by comparing the red dashed curve (x -component) to the blue and green curves (y - and z -components).

The time evolution of the magnetic energy wavenumber spectra is shown in Fig. 1b. After $t = 0$, where the magnetic field is seeded only up to $k/k_0 = 4$, the first time point shown is already after the Weibel phase, and its high- k range is dominated by a peak corresponding to magnetic energy created by the Weibel instability. The spectral peak then moves towards lower k , until the magnetic energy at the lowest wave number ($k = k_0$) takes over. Eventually, most of the spectrum becomes power-law-like, comparable to $k^{-5.5}$ (as indicated by the dotted line), while the lowermost k range, up to around $4k_0$, exhibits a less steep spectrum, approximately $k^{-1.6}$.

The dynamics of the system during the short Weibel period is illustrated in Fig. 2a, which contains similar information to Fig. 2 of (Zhou *et al.* 2022). The magnetic energy,

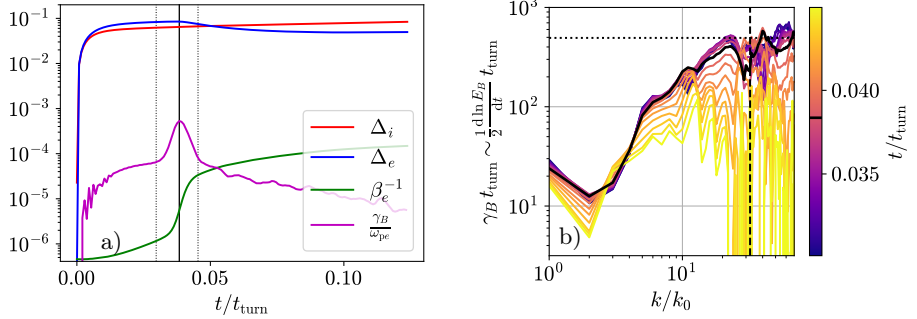


FIGURE 2. Time evolution during the Weibel instability phase. a) Dimensionless quantities: Pressure anisotropy of electrons (blue, Δ_e) and ions (red, Δ_i), normalized magnetic field energy (green, β_e^{-1}), and instantaneous magnetic field growth rate (purple, γ_B/ω_{pe}). b) Instantaneous magnetic growth rate spectra ($\gamma_B t_{\text{turn}}$) for several time instances (color coded from blue to yellow for increasing time) across the time period of the fastest field growth, bound by the dotted vertical lines of panel a). The black curve corresponds to the time of fastest global magnetic field growth, indicated by the solid vertical line in panel a). The dotted horizontal and the dashed vertical line correspond to $\gamma_B = \Delta_e^{3/2} \omega_{pe} v_{\text{th},e} / c$ and $k = \Delta_e^{1/2} / \delta_e$, respectively.

now quantified via β_e^{-1} (green curve) undergoes a very rapid growth phase approximately bounded by the dotted vertical lines, with the instantaneous growth rate of the magnetic field (γ_B , purple) peaking just before $t/t_{\text{turn}} = 0.04$, marked by the solid line. Initially the pressure anisotropies of both species are growing in accordance with the sheared flow that is present in the system already from $t = 0$. When the growth rate peaks, the instability becomes strong enough that it starts to back-react on its drive, the electron pressure anisotropy (Δ_e , blue). Δ_e declines somewhat to eventually stabilize at a lower level. Meanwhile, the steady growth of the ion pressure anisotropy (Δ_i , red) remains unaffected by the instability, providing one piece of evidence that the instability is indeed driven by Δ_e . More details on the evolution of the system in terms of electron pressure anisotropy and normalized pressure are provided in Appendix B.

The wave number-resolved instantaneous growth rates of the magnetic field are shown for a range of time points in Fig. 2b. At the approximate time of fastest global magnetic energy growth, corresponding to the thick black line, the peak of the growth rate spectrum is located in the vicinity of $k = \Delta_e^{1/2} / \delta_e$ and takes a value comparable to $\gamma_B = \Delta_e^{3/2} \omega_{pe} v_{\text{th},e} / c$, indicated by the dashed vertical and the dotted horizontal lines respectively. These are the theoretical scalings from (Zhou *et al.* 2023), without their specific order unity prefactors. The purpose of these is just to illustrate that the magnetic field growth is consistent with being produced by the electron Weibel instability. An accurate numerical comparison would require theory for a system similar to our simulated scenario, but even then, differences due to our simulation being fluid are expected.

The morphology of the magnetic field strength is shown in Fig. 3 for the three phases of the magnetic field evolution. The left panels, taken at the time of fastest magnetic growth in the Weibel phase, show characteristic Weibel filamentation is coincident with the regions of strongest shear in the GP flow structure (stream plotted with white arrows). Recall from Eq. (2.6) that the flow is independent of x , and it forms two circulations in the y - z plane around the elliptic fixed points located at $\{z, y\} \approx \{0.25, 0.84\}$ and $\{z, y\} \approx \{0.75, 0.34\}$. In these nearly circular regions, the magnetic field remains relatively low, with some structure around the boundary of the circulations, as shown in Fig. 3a.

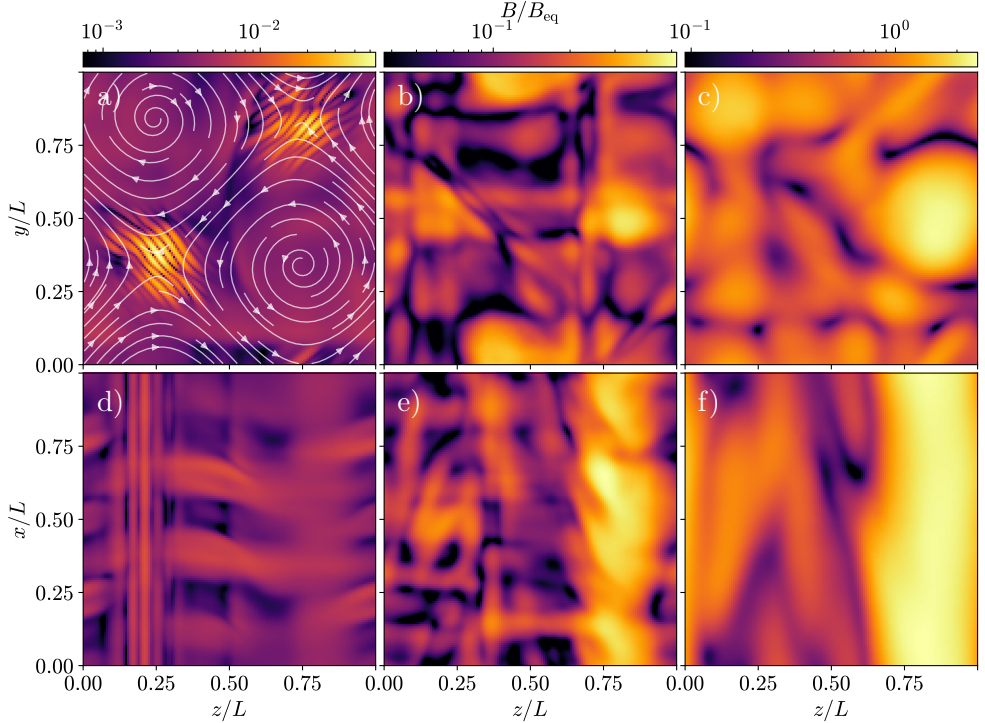


FIGURE 3. Magnitude of the magnetic field in 2-D cuts of the simulation domain, taken a) and d) at the time of the fastest magnetic growth during the Weibel phase, $t/t_{\text{turn}} = 0.038$, b) and e) in the middle of the dynamo growth phase, $t/t_{\text{turn}} = 2.0$, and c) and f) in the saturated phase, $t/t_{\text{turn}} = 10.0$. a)-c) are cuts at $x = L/2$, while d)-f) are cuts at $y = L/2$ (the latter are morphologically similar to constant z cuts, not shown). The normalizing, ‘‘equipartition’’ magnetic field B_{eq} is defined such that $B_{\text{eq}}^2/(2\mu_0)$ equals the box-averaged kinetic energy density in the bulk flows at $t = 0$.

The strongest magnetic energy growth is instead observed in the vicinity of the hyperbolic fixed points located around $\{z, y\} \approx \{0.25, 0.34\}$ and $\{z, y\} \approx \{0.75, 0.84\}$. It is in fact in these regions where the shear strain of the flow is strongest†. In this z - y plane, the magnetic filaments are aligned parallel to the unstable separatrix. In the z - x plane, Fig. 3d, the same filaments, which form planar structures in three dimensions, are elongated along the x direction, best seen around $z = 0.25$, which is close to one of the highly strained regions. In the rest of the plane, the striations are elongated mostly in the z direction; they have longer wavelengths and are caused by the sheared flows in the x -direction.

In the dynamo growth phase, shown in Fig. 3b and e, the localized fine scale striations corresponding to the electron Weibel instability disappear, and no clear directionality is left in the z - y plane. The characteristic scale of the fluctuations is clearly larger than that of the Weibel striations. Due to the special form of the flow forcing, the fluctuations are not completely isotropic even in the z - y plane, rather some structure appears to be

† Quantitatively, these hyperbolic fixed-point areas produce the highest negative values of the Q-parameter, also referred to as the second invariant of the flow gradient tensor (Chong *et al.* 1990).

aligned with the coordinate axes. This preferential alignment in the z - y plane is not apparent in the saturated state, shown in Fig. 3c and f. However, there is an alignment with the special direction x , which, being a symmetry direction of the forcing, consistently supports the strongest flows (as also seen by comparing the corresponding flow energies: the red dashed curve to the blue and green ones in Fig. 1a).

3.2. Increased electron pressure isotropization

We will now consider the effect of increasing electron pressure isotropization from its baseline value $k_{0,e}/k_0 = 1$. Information similar to that in Fig. 1, but for $k_{0,e}/k_0 = \{2, 4, 8, 32\}$, is shown in Fig. 4. As the strength of the isotropization is increased, and thus the drive of the Weibel instability is reduced, we observe a diminishing Weibel growth phase. Up to the $k_{0,e}/k_0 = 4$ case, we still observe a magnetic growth rate that increases in time during the otherwise nearly exponential dynamo growth phase, but it is not present in the higher $k_{0,e}$ cases. Perhaps more importantly, the representative growth rate increases with increasing $k_{0,e}$, as indicated by the dotted lines and $\gamma_B t_{\text{turn}}$ values in the figure. This behavior is consistent with the magnetic damping decreasing as $1/k_{0,e}$. To draw an analogy with the dynamo in resistive magnetohydrodynamics, we may think of the reduced magnetic damping as an increased magnetic Reynolds number. A fast dynamo produces an increasing, and eventually saturated growth rate with increasing magnetic Reynolds number, which is qualitatively consistent with the increasing γ_B we observe for increasing $k_{0,e}$.

Similar to the $k_{0,e}/k_0 = 1$ case, when the magnetic field energy reaches dynamically significant levels, it back-reacts on the flow, leading to a temporary reduction of the flow energy. Eventually, the flow energy grows back to nearly its initial value, and the two forms of energy reach near equipartition. Again, due to the type of flow we drive, the x component of both the flow and the magnetic energy provide the largest contribution to the respective energies (red lines).

The diminishing Weibel phase with increasing $k_{0,e}$ is also reflected in the magnetic energy spectra, where the pronounced Weibel peak seen for $k_{0,e}/k_0 = 1$ is not clearly present anymore. The magnetic spectra develop similarly strong dependence on k as the $k_{0,e}/k_0 = 1$ case, and no clear trend is observed in terms of the spectral shape as $k_{0,e}$ is increased. The spectra appear to exhibit two changes in slope (most clearly seen in the $k_{0,e}/k_0 = 8$ case), with the intermediate range displaying the steepest spectral index. However, given the limited spatial-scale separation and available statistics, this feature should be interpreted with caution.

4. Summary and discussion

Recent progress in understanding magnetic-field generation in large, weakly collisional astrophysical systems has demonstrated the need to capture physics beyond magnetohydrodynamics. At the same time, fully kinetic investigations remain severely constrained in both parameter coverage and dynamic range due to the extreme numerical demands of this inherently three-dimensional, multiscale problem. Here, we leverage the capabilities of the 10-moment collisionless fluid solver of `Gkeyll` to provide an alternative approach to the problem, with physics fidelity and computational complexity between the mentioned extremes. The model allows us to perform simulations, at modest numerical expense, that bridge the spatiotemporal scales between seed generation by the electron Weibel instability and a subsequent, saturating dynamo process, at a mass ratio well above unity and a non-relativistic temperature.

The results are qualitatively similar to previous fully kinetic simulations performed in a

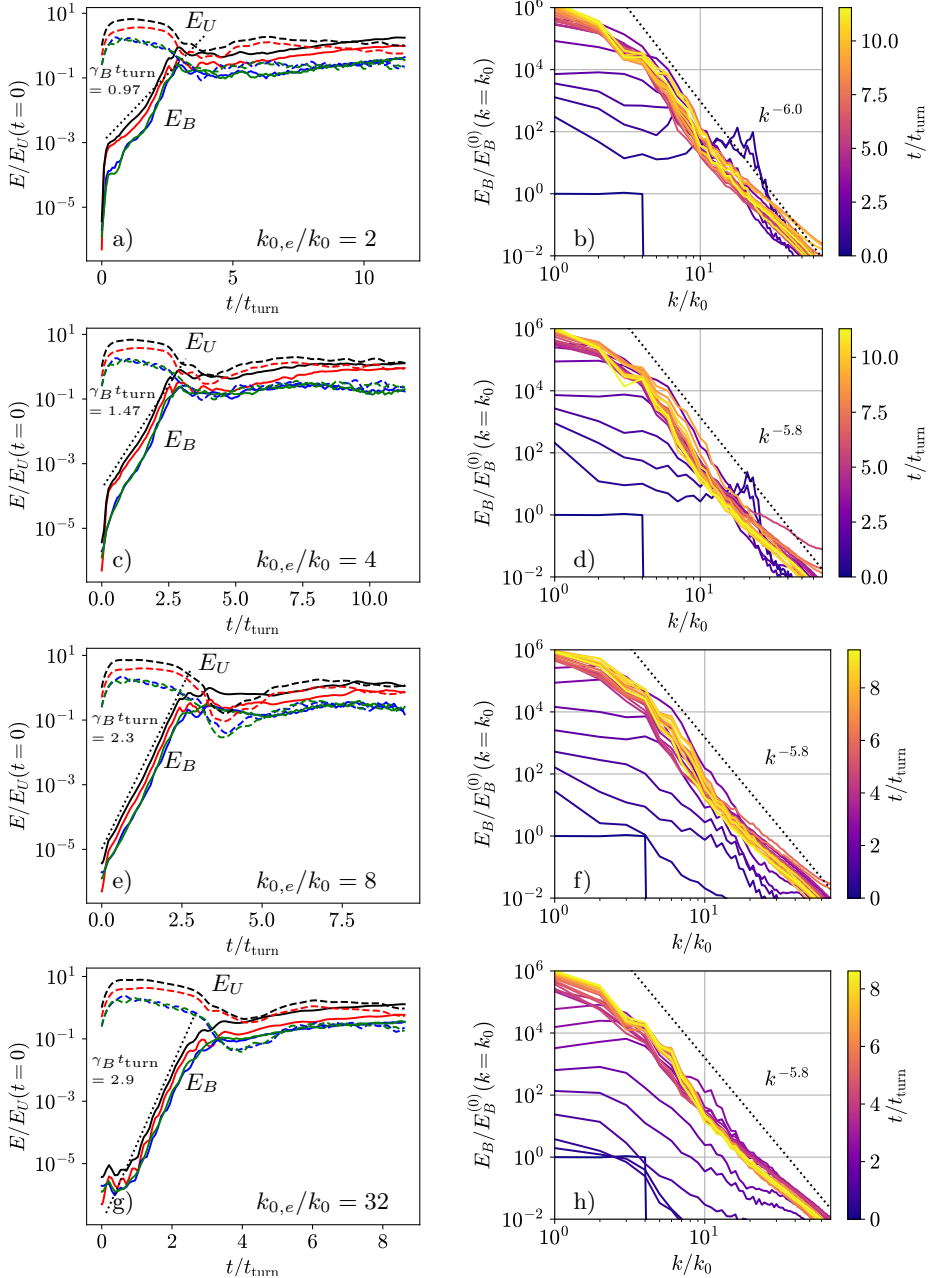


FIGURE 4. Magnetic field generation in simulations using $k_{0,e}/k_0 = \{2, 4, 8, 32\}$, shown in different rows. Left column: Time evolution of the box-integrated magnetic energy E_B (solid black curve) and kinetic energy in the flows E_U (dashed black), normalized to the initial value of E_U . With similar line styles, contributions from the $\{x, y, z\}$ components of \mathbf{U} and \mathbf{B} are shown in red, blue and green, respectively. Exponential magnetic growth is indicated by dotted lines with growth rates provided in the figure. Right column: Wave number spectra of the magnetic field energy. The wave number k is normalized to k_0 and the spectra are normalized to its value at $k = k_0$ for $t = 0$. Dotted lines indicate power laws for reference.

pair plasma. The process starts with a distinct phase dominated by Weibel magnetic field growth, destabilized by electron pressure anisotropy that, in turn, is generated by phase mixing of sheared flows. The phase is followed by dynamo growth of the magnetic energy on outer-turnover timescales, saturating at dynamically significant levels, in equipartition with the kinetic energy in the bulk flow. However, unlike pair-plasmas, the role of the two particle species is clearly separated: The first sign of this is that the electron Weibel instability only regulates the electron pressure anisotropy upon saturation, while it leaves the ion anisotropy unaffected. More generally, as shown in Appendix A, the scale-dependent damping of the mass flow is determined by the ion heat flux as the mass flow is dominantly carried by the ions, while the magnetic field damping is governed by the electron heat flux as the currents are mostly carried by electrons.

In the 10-moment model, the heat fluxes are not self-consistent, rather they are provided by a closure model. In particular, we use the pressure isotropization closure, with one free parameter per species, $k_{0,\alpha}$. These free parameters then control the damping of flows and magnetic fields. The flow damping caused by this heat flux model is found to be diffusive ($\propto k^2$), in analogy with viscous damping, and the magnetic field damping is superdiffusive ($\propto k^4$). By adjusting $k_{0,e}$ and $k_{0,i}$ we can explore various effective magnetic and fluid Reynolds numbers. We target $\text{Re} < 1$ and $\text{Rm} \gg 1$, to be relevant to intracluster media.

Increasing the electron isotropization strength $k_{0,e}$ and thereby the effective Rm value (as the magnetic field damping is inversely proportional to $k_{0,e}$), we observe increasing dynamo growth rates, similar to fast dynamos in resistive MHD. In addition, the simulations become more MHD-like as $k_{0,e}$ is increased, in the sense that the pressure remains nearly isotropic, and as a consequence, the Weibel phase diminishes in length.

Adopting the 10-moment modeling approach opens up several avenues for further investigation. Here, we started to explore the effect of the free parameters of the heat flux closures; however, these may instead be fixed such as to optimally account for some aspects of the physics, such as accurately capturing the wave number spectrum or the saturation level of the Weibel instability. Improving the heat flux closure model through e.g., theoretical (Hammett & Perkins 1990) or data driven approaches (Ingelsten *et al.* 2025; Huang *et al.* 2025; Barbour *et al.* 2025) would allow a more accurate representation of some physical process deemed to be of central importance.

The reduced computational cost compared to the kinetic approach enables a dedicated study of mass-ratio effects, providing an essential input for extrapolating these results to the physical mass ratio of an electron-proton plasma. The accuracy and the possibilities to capture various kinetic effects can be enhanced by representing various particle populations (e.g., hot and cold) as separate species, with only a limited increase in computational complexity. The larger numerical flexibility is also beneficial for improving the realism of the turbulence driver, by e.g., modeling gravitational collapse with a dark matter component that is only gravitationally coupled to the plasma.

Acknowledgments

The authors are grateful to Muni Zhou for a fruitful discussion, as well as Sarah Newton and Tünde Fülöp for constructive comments on the manuscript. The computations were enabled by resources provided by the National Academic Infrastructure for Supercomputing in Sweden (NAISS), partially funded by the Swedish Research Council through grant agreement No. 2022-06725. The authors also acknowledge the Texas Advanced Computing Center (TACC) at The University of Texas at Austin for

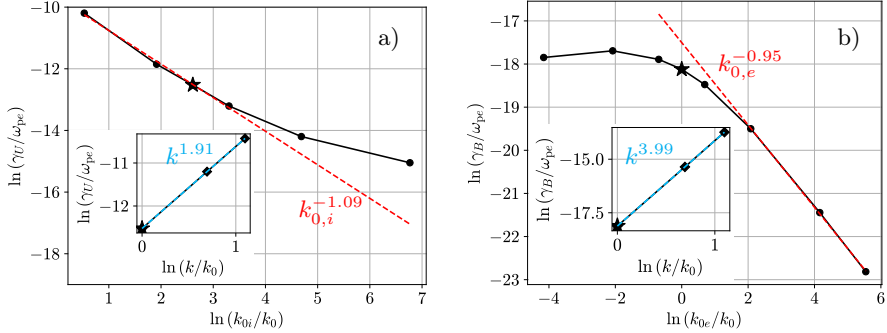


FIGURE 5. Dependence of damping rates on closure parameters (circle markers, main figure) and wavenumber (diamond markers, inset figure). In both of these scans, star markers correspond to the baseline case. Dashed lines indicate fitted relevant power-law behavior. a) Mass flow damping rate as a function of $k_{0,i}/k_0$ and k/k_0 . b) Magnetic field damping rate as a function of $k_{0,e}/k_0$ and k/k_0 .

providing computational resources that have contributed to the research results reported within this paper.

Funding

The work was supported by the Swedish Research Council (Dnr. 2021-03943) and the Knut and Alice Wallenberg foundation (Dnr. 2022.0087). J. Juno, A. Hakim, J. M. TenBarge, and the development of `Gkeyll` were partly funded by the NSF-CSSI program, Award No. 2209471. J. Juno and A. Hakim were also supported by the U.S. Department of Energy under Contract No. DE-AC02-09CH1146 via LDRD grants. J. M. TenBarge was also supported by NASA grant 80NSSC23K0099.

Declaration of Interests

Competing interests: The authors declare none.

Appendix A. The effect of closure parameters on magnetic field and flow damping

To establish how the damping of the mass flows and magnetic fields depend on the closure parameters, we have performed one dimensional simulations initialized with small amplitude, sinusoidally varying, divergence-free perturbations of the respective quantities. The self-consistent exponential decay of these perturbations was used to fit flow and magnetic decay rates, γ_U and γ_B . In particular, for the mass flow decay studies, the only non-vanishing component of the (equal) ion and electron flows are initially $u_{\alpha z} = u_{\alpha z0} \sin(kx)$. For the magnetic decay studies only the electrons have a non-zero initial velocity of the same form with a flow amplitude $u_{ez0} = B_{y0}k/(e\mu_0 n_e)$, corresponding to a magnetic field perturbation $B_y = B_{y0} \cos(kx)$. These simulations use the same linear box size as our dynamo simulations (namely, L that defines $k_0 = 2\pi/L$ used for normalization), while employing 10 times higher resolution for improved accuracy.

Figure 5 illustrates the numerically obtained dependencies of the damping rates in the vicinity of our baseline parameters. Over certain ranges, both γ_U and γ_B are

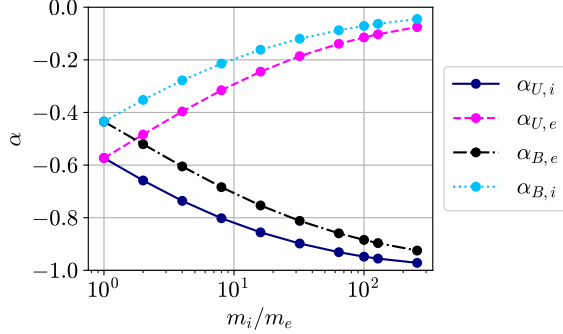


FIGURE 6. Mass-ratio dependence of the damping rate scaling exponents, defined through the power law relations $\gamma_U \propto k_{0,i}^{\alpha_{U,i}} k_{0,e}^{\alpha_{U,e}}$, $\gamma_B \propto k_{0,i}^{\alpha_{B,i}} k_{0,e}^{\alpha_{B,e}}$.

approximately inversely proportional to their respective closure parameter: $\gamma_U \propto k_{0,i}^{-1}$ and $\gamma_B \propto k_{0,e}^{-1}$. For the flow damping, this dependence can be understood by a linearized analysis, with the assumptions that in the momentum equation the $m_i n_i \partial_t u_{iz}$ and $\partial_x p_{ixz}$ terms nearly balance, while in the relevant xz component of the pressure tensor equation, the generation of this off-diagonal pressure component by the term $p_{ixx} \partial_x u_{iz}$ is nearly compensated by its destruction by the isotropizing closure term $v_{th,i} k_{0,i} p_{ixz}$. This behavior yields a dependence of the damping rate $\gamma_U \propto v_{th,i} k^2 / k_{0,i}$, consistent with the scalings found in simulations around the baseline point. A somewhat more involved calculation of the magnetic damping rate, where Maxwell's equations are also invoked in addition to the fluid ones, yields a similar regime $\gamma_B \propto v_{th,e} k^4 \delta_e^2 / k_{0,e}$. We note that this differs from the exact kinetic damping of magnetic fields (Mikhailovskii 1980; Pusztai *et al.* 2020) that is of the form $\gamma_B \propto v_{th,e} k^3 \delta_e^2$; thus our closure introduces an extra $k/k_{0,e}$ factor.

Clearly, the $1/k_{0,\alpha}$ scaling cannot hold for arbitrarily low values of the closure coefficients $k_{0,\alpha}$, because at low values, the damping rates saturate at a finite value. This behavior can be seen for γ_B in Fig. 5b. In fact, box-scale magnetic perturbations at our baseline parameters are in the transition region to this saturation (while higher k values are typically in the $\gamma_B \propto k_{0,e}^{-1}$ regime). However, increasing $k_{0,e}$ brings our simulations away from this saturation, providing a reduced magnetic damping, which is essential for the interpretation of the dynamo results. Concerning flow damping, we observe the damping rate to level off also at high values of $k_{0,i}$, and our baseline case is in this vicinity. It is of no concern though, as we do not perform scans in this closure parameter.

The effect of the mass ratio on the scaling of the damping rates is illustrated in Fig. 6 in terms of the exponents defined by

$$\gamma_U \propto k_{0,i}^{\alpha_{U,i}} k_{0,e}^{\alpha_{U,e}} k^{\alpha_{U,k}}, \quad \gamma_B \propto k_{0,i}^{\alpha_{B,i}} k_{0,e}^{\alpha_{B,e}} k^{\alpha_{B,k}}. \quad (\text{A } 1)$$

We consider a working point with parameters $k = k_0$ and $k_{0,i} = 13.6k_0$, as in our baseline case, and set $k_{0,e} = 13.6k_0$ to ensure consistency at unit mass ratio. The quantities $k_{0,i}$, $k_{0,e}$, and k are then perturbed about their baseline values in magnetic-field and mass-flow damping tests to determine the above exponents. In all simulations, the electron mass is held fixed while the ion mass is varied.

The exponents characterizing the k dependence remain nearly constant over the entire mass-ratio scan, with $\alpha_{U,k} \approx 2$ and $\alpha_{B,k} \approx 4$, exhibiting maximum deviations of only 1.2% and 0.05%, respectively. As these variations are negligible, the corresponding

exponents are omitted from the figure. At unit mass ratio, the effects of ion (or, in this case, positron) and electron closures on the damping of a given quantity are identical, as expected. As the mass ratio increases, $\alpha_{U,i}$ and $\alpha_{B,e}$ approach -1 , while $\alpha_{U,e}$ and $\alpha_{B,i}$ approach 0 . In other words, at sufficiently large mass ratio, magnetic-field damping depends solely on $k_{0,e}$, whereas mass-flow damping depends solely on $k_{0,i}$, with cross-dependencies becoming negligible. This decoupling between electron and ion closures is already well converged at the mass ratio used in this study, $m_i/m_e = 100$.

Finally, we note that over the mass-ratio range considered here, the sums $\alpha_{B,i} + \alpha_{U,i}$ and $\alpha_{B,e} + \alpha_{U,e}$ remain close to -1 , with maximum deviations of 1.9% and 0.8% , respectively.

Appendix B. Evolution of pressure anisotropy and normalized pressure

High beta systems where pressure anisotropy driven instabilities are active are often analyzed in terms of their distribution in $p_{\perp,e}/p_{\parallel,e} - \beta_{\parallel}$ space. The distribution may then be effectively limited by stability boundaries (Bale *et al.* 2009). Such figures are often referred to as *Brazil plots* due to the characteristic shape of the instability-limited distributions. We show such distributions in Fig. 7 at three representative time points in the Weibel, the kinematic, and the saturated phase (the same time points as in Fig. 3). The vertical lines indicate magnetic field values for which $\beta_{e,\parallel}$ is calculated with the initial $p_{e,\parallel}$. Note that now we show the pressure with components parallel and perpendicular to the magnetic field, even though electrons never get very strongly magnetized. Accordingly, $p_{e,\perp}$ is the average of the generally unequal pressure components perpendicular to the local field direction.

In the first time point shown, thermal electrons are just becoming magnetized at the box scale, indicated by the $\rho_e = L$ vertical line. Note that well into the dynamo phase, shown by the middle panels, most of the electrons are still far from being magnetized at the spatial scale where the peak of the magnetic spectrum corresponding to the Weibel instability was located (marked by the $\rho_e = k_{\text{Weibel}}^{-1}$). That is, the saturation of the Weibel instability is not caused by the electrons becoming magnetized at the characteristic Weibel instability scales. Due to the small pressure anisotropies achieved here, the Weibel saturation mechanism is in its Alfvén current regime according to the classification introduced by Kato (2005). This limit yields lower saturation field amplitudes, corresponding to $\beta_{e,\parallel} \approx 1.3 \times 10^3$ in our simulation, in good agreement with what we observe at the highest B region upon saturation.

At the final time step (right panels), we observe that the β_e distribution is effectively limited by equipartition between the energy of the magnetic field and the bulk flows (the latter being calculated at its initial value, which remains representative in the saturated phase).

Notably, as seen by comparing the upper and lower panels, the pressure anisotropies achieved are significantly affected by the closure parameter $k_{0,e}$, somewhat unsurprisingly since the closure drives the system towards isotropic pressure. Without such regularization (lower panels), non-negligible pressure anisotropies can develop during the Weibel instability phase, as the instability has not started to saturate yet; see Fig. 7d. During the dynamo growth phase, some fraction of the plasma gains even higher anisotropies, especially at lower beta values, see Fig. 7e, with the anisotropy decreasing towards higher $\beta_{e,\parallel}$ values, reminiscent of typical Brazil plots. However, here, the significant anisotropy values reached appear at unusually high (i.e., higher than order unity) $\beta_{e,\parallel}$ values. This indicates that, in this phase of the simulation, the effective pitch-angle scattering rate caused by pressure anisotropy driven high-beta instabilities is not sufficiently high to

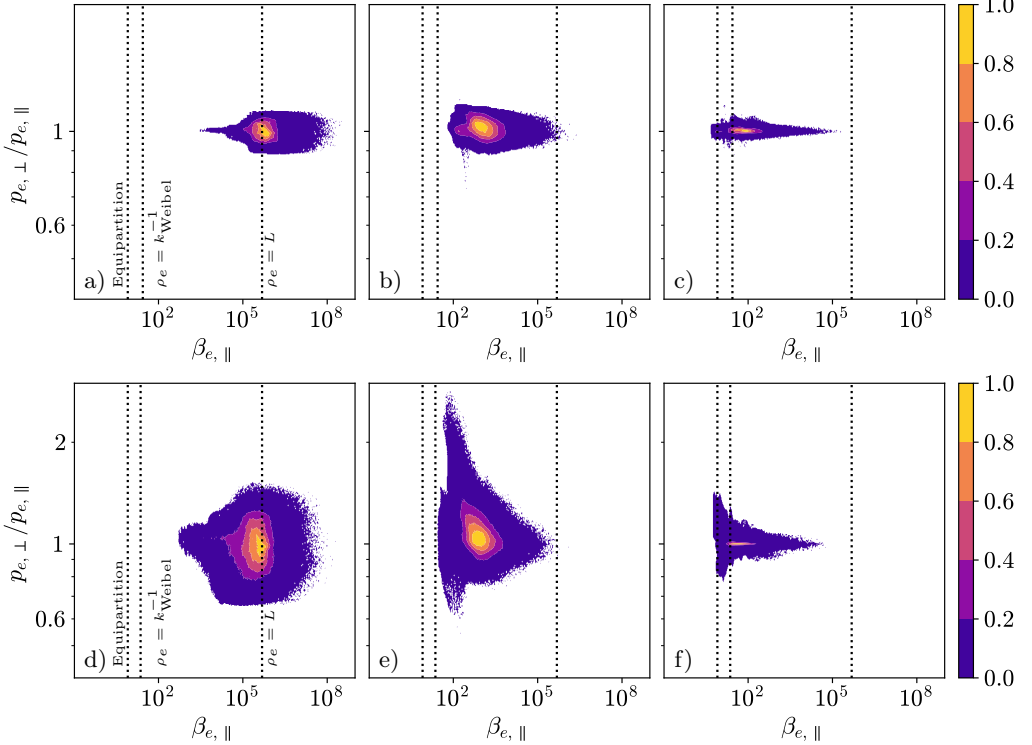


FIGURE 7. Normalized probability distributions of $p_{\perp,e}/p_{\parallel,e}$ and β_{\parallel} at three representative time points. Left panels: time of fastest Weibel growth ($t/t_{\text{turn}} = 0.038$ and $t/t_{\text{turn}} = 0.021$ respectively); middle panels: $t/t_{\text{turn}} = 2.0$ (kinematic dynamo phase), right panels: $t/t_{\text{turn}} = 10.0$ (saturated dynamo phase). The electron closure parameter is changed from its baseline value $k_{0,e} = 1k_0$ (upper panels) to a negligible value $10^{-6}k_0$ (lower panels; note the slightly different y-axis scales). Vertical dotted lines indicate specific magnetic field strength values in terms of $\beta_{e,\parallel}$.

pin the anisotropy to stability limits. This is consistent with observations in dynamo simulations performed for pair plasmas kinetically by Zhou *et al.* (2023), and also similar to the kinetic ion dynamics in hybrid simulations of St-Onge & Kunz (2018).

In the saturated phase (right panels), the pressure anisotropy is significantly reduced compared to the growth phase, for both $k_{0,e}$ values. This behavior indicates an effective pitch angle scattering, even though most of the electrons are magnetized by the large-scale magnetic fields. The scattering may be due to instabilities, as well as a magnetic field line geometry exhibiting sharp turns acting as scattering centers Walters *et al.* (2024); Rosin *et al.* (2011).

REFERENCES

AMANO, TAKANOBU, MATSUMOTO, YOSUKE, BOHDAN, ARTEM, KOBZAR, OLEH, MATSUKIYO, SHUICHI, OKA, MITSUO, NIEMIEC, JACEK, POHL, MARTIN & HOSHINO, MASAHIRO 2022 Nonthermal electron acceleration at collisionless quasi-perpendicular shocks. *Reviews of Modern Plasma Physics* **6** (1), 29.

BALE, S. D., KASPER, J. C., HOWES, G. G., QUATAERT, E., SALEM, C. & SUNDKVIST, D. 2009 Magnetic fluctuation power near proton temperature anisotropy instability thresholds in the solar wind. *Phys. Rev. Lett.* **103**, 211101.

BARBOUR, NATHANIEL, DORLAND, WILLIAM, ABEL, IAN G. & LANDREMAN, MATT 2025

Machine-learning closure for vlasov–poisson dynamics in fourier–hermite space. *Journal of Plasma Physics* **91** (5), E140.

BIERMANN, L. 1950 Über den ursprung der magnetfelder auf sternen und im interstellaren raum. *Zeitschrift für Naturforschung A* **5** (2), 65–71.

BONAFEDE, A., FERETTI, L., MURGIA, M., GOVONI, F., GIOVANNINI, G., DALLACASA, D., DOLAG, K. & TAYLOR, G. B. 2010 The coma cluster magnetic field from faraday rotation measures. *Astronomy and Astrophysics* **513**, A30.

BRANDENBURG, AXEL & NTORMOUSI, EVANGELIA 2023 Galactic dynamos. *Annual Review of Astronomy and Astrophysics* **61** (Volume 61, 2023), 561–606.

BRANDENBURG, AXEL & SUBRAMANIAN, KANDASWAMY 2005 Astrophysical magnetic fields and nonlinear dynamo theory. *Physics Reports* **417** (1), 1–209.

CALIFANO, F., PEGORARO, F., BULANOV, S. V. & MANGENEY, A. 1998 Kinetic saturation of the weibel instability in a collisionless plasma. *Phys. Rev. E* **57**, 7048–7059.

CARILLI, C. L. & TAYLOR, G. B. 2002 Cluster magnetic fields. *Annual Review of Astronomy and Astrophysics* **40** (Volume 40, 2002), 319–348.

CHONG, M. S., PERRY, A. E. & CANTWELL, B. J. 1990 A general classification of three-dimensional flow fields. *Physics of Fluids A: Fluid Dynamics* **2** (5), 765–777.

CRUTCHER, RICHARD M. 2012 Magnetic fields in molecular clouds. *Annual Review of Astronomy and Astrophysics* **50** (Volume 50, 2012), 29–63.

DURRIVE, J.-B. & LANGER, M. 2015 Intergalactic magnetogenesis at cosmic dawn by photoionization. *Monthly Notices of the Royal Astronomical Society* **453** (1), 345–356, arXiv: <https://academic.oup.com/mnras/article-pdf/453/1/345/4913470/stv1578.pdf>.

FERETTI, LUIGINA, GIOVANNINI, GABRIELE, GOVONI, FEDERICA & MURGIA, MATTEO 2012 Clusters of galaxies: observational properties of the diffuse radio emission. *The Astronomy and Astrophysics Review* **20** (1), 54.

GALLOWAY, D. J. & PROCTOR, M. R. E. 1992 Numerical calculations of fast dynamos in smooth velocity fields with realistic diffusion. *Nature* **356** (6371), 691–693.

GARY, S PETER 1993 *Cambridge atmospheric and space science series: Theory of space plasma microinstabilities*. Cambridge, England: Cambridge University Press.

GOVONI, FEDERICA & FERETTI, LUIGINA 2004 Magnetic fields in clusters of galaxies. *International Journal of Modern Physics D* **13** (08), 1549–1594, arXiv: <https://doi.org/10.1142/S0218271804005080>.

GUO, FAN, LIU, YI-HSIN, ZENITANI, SEIJI & HOSHINO, MASAHIRO 2024 Magnetic reconnection and associated particle acceleration in high-energy astrophysics. *Space Science Reviews* **220** (4), 43.

HAMMETT, GREGORY W. & PERKINS, FRANCIS W. 1990 Fluid moment models for landau damping with application to the ion-temperature-gradient instability. *Phys. Rev. Lett.* **64**, 3019–3022.

HELANDER, P., STRUMIK, M. & SCHEKOCHIHIH, A. A. 2016 Constraints on dynamo action in plasmas. *Journal of Plasma Physics* **82** (6), 905820601.

HUANG, ZIYU, DONG, CHUANFEI & WANG, LIANG 2025 Machine-learning heat flux closure for multi-moment fluid modeling of nonlinear landau damping. *Proceedings of the National Academy of Sciences* **122** (11), e2419073122.

HUNTINGTON, C. M., FIUZA, F., ROSS, J. S., ZYLSTRA, A. B., DRAKE, R. P., FROUZA, D. H., GREGORI, G., KUGLAND, N. L., KURANZ, C. C., LEVY, M. C., LI, C. K., MEINECKE, J., MORITA, T., PETRASSO, R., PLECHATY, C., REMINGTON, B. A., RYUTOV, D. D., SAKAWA, Y., SPITKOVSKY, A., TAKABE, H. & PARK, H.-S. 2015 Observation of magnetic field generation via the weibel instability in interpenetrating plasma flows. *Nature Physics* **11** (2), 173–176.

INGELSTEN, EMIL R., MCGRAE-MENGE, MADOX C., ALVES, E. PAULO & PUSZTAI, ISTVAN 2025 Data-driven discovery of a heat flux closure for electrostatic plasma phenomena. *Journal of Plasma Physics* **91** (2), E64.

KÄPYLÄ, PETRI J., BROWNING, MATTHEW K., BRUN, ALLAN SACHA, GUERRERO, GUSTAVO & WARNECKE, JÖRN 2023 Simulations of solar and stellar dynamos and their theoretical interpretation. *Space Science Reviews* **219** (7), 58.

KATO, TSUNEHICO N. 2005 Saturation mechanism of the weibel instability in weakly magnetized plasmas. *Physics of Plasmas* **12** (8), 080705.

KATO, TSUNEHICO N. & TAKABE, HIDEAKI 2008 Nonrelativistic collisionless shocks in unmagnetized electron-ion plasmas. *The Astrophysical Journal* **681** (2), L93.

KOMAROV, S., SCHEKOCHIHIH, A. A., CHURAZOV, E. & SPITKOVSKY, A. 2018 Self-inhibiting thermal conduction in a high- β , whistler-unstable plasma. *Journal of Plasma Physics* **84** (3), 905840305.

KOMAROV, S. V., CHURAZOV, E. M., KUNZ, M. W. & SCHEKOCHIHIH, A. A. 2016 Thermal conduction in a mirror-unstable plasma. *Monthly Notices of the Royal Astronomical Society* **460** (1), 467–477.

KORPI-LAGG, MAARIT J., MAC LOW, MORDECAI-MARK & GENT, FREDERICK A. 2024 Computational approaches to modeling dynamos in galaxies. *Living Reviews in Computational Astrophysics* **10** (1), 3.

KULDINOW, D.A. & HARA, K. 2025 Ten-moment fluid modeling of the weibel instability. *Journal of Plasma Physics* **91** (2), E66.

KULSRUD, RUSSELL M. & ZWEIBEL, ELLEN G. 2008 On the origin of cosmic magnetic fields. *Reports on Progress in Physics* **71** (4), 046901.

KUNZ, MATTHEW W., SCHEKOCHIHIH, ALEXANDER A. & STONE, JAMES M. 2014 Firehose and mirror instabilities in a collisionless shearing plasma. *Phys. Rev. Lett.* **112**, 205003.

LANGER, MATHIEU & DURRIVE, JEAN-BAPTISTE 2018 Magnetizing the cosmic web during reionization. *Galaxies* **6** (4), 124.

LARMOR, J. 1919 Possible rotational origin of magnetic fields of sun and earth. *Engineering Review* **108**, 461ff.

LEVEQUE, RANDALL J. 1997 Wave propagation algorithms for multidimensional hyperbolic systems. *Journal of Computational Physics* **131** (2), 327–353.

LIU, ZHUO, ZHOU, MUNI & LOUREIRO, NUNO F. 2025 Suppression of inverse magnetic energy transfer in collisionless marginally magnetized plasmas. *The Astrophysical Journal Letters* **995** (2), L46.

MATTHEWS, JAMES H., BELL, ANTHONY R. & BLUNDELL, KATHERINE M. 2020 Particle acceleration in astrophysical jets. *New Astronomy Reviews* **89**, 101543.

MEDVEDEV, MIKHAIL V. & LOEB, ABRAHAM 1999 Generation of magnetic fields in the relativistic shock of gamma-ray burst sources. *The Astrophysical Journal* **526** (2), 697.

MEDVEDEV, MIKHAIL V., SILVA, LUIS O. & KAMIONKOWSKI, MARC 2006 Cluster magnetic fields from large-scale structure and galaxy cluster shocks. *The Astrophysical Journal* **642** (1), L1.

MIKHAILOVSKII, A. B. 1980 Oscillations of an isotropic relativistic plasma. *Plasma Physics* **22** (2), 133.

NG, JONATHAN, HAKIM, AMMAR, BHATTACHARJEE, A., STANIER, ADAM & DAUGHTON, W. 2017 Simulations of anti-parallel reconnection using a nonlocal heat flux closure. *Physics of Plasmas* **24** (8), 082112.

NG, JONATHAN, HAKIM, A., WANG, L. & BHATTACHARJEE, A. 2020 An improved ten-moment closure for reconnection and instabilities. *Physics of Plasmas* **27** (8), 082106.

PORTER, DAVID H., JONES, T. W. & RYU, DONGSU 2015 Vorticity, shocks, and magnetic fields in subsonic, icm-like turbulence. *The Astrophysical Journal* **810** (2), 93.

PUCCI, F., VIVIANI, M., VALENTINI, F., LAPENTA, G., MATTHAEUS, W. H. & SERVIDIO, S. 2021 Turbulent magnetogenesis in a collisionless plasma. *The Astrophysical Journal Letters* **922** (1), L18.

PUSZTAI, ISTVÁN, JUNO, JAMES, BRANDENBURG, AXEL, TENBARGE, JASON M., HAKIM, AMMAR, FRANCISQUEZ, MANAURE & SUNDSTRÖM, ANDRÉAS 2020 Dynamo in weakly collisional nonmagnetized plasmas impeded by landau damping of magnetic fields. *Phys. Rev. Lett.* **124**, 255102.

RINCON, FRANÇOIS 2019 Dynamo theories. *Journal of Plasma Physics* **85** (4), 205850401.

RINCON, FRANÇOIS, CALIFANO, FRANCESCO, SCHEKOCHIHIH, ALEXANDER A. & VALENTINI, FRANCESCO 2016 Turbulent dynamo in a collisionless plasma. *Proceedings of the National Academy of Sciences* **113** (15), 3950–3953, arXiv: <https://www.pnas.org/doi/pdf/10.1073/pnas.1525194113>.

ROBERG-CLARK, G. T., DRAKE, J. F., REYNOLDS, C. S. & SWISDAK, M. 2016 Suppression of electron thermal conductionin the high β intracluster medium of galaxy clusters. *The Astrophysical Journal Letters* **830** (1), L9.

ROBERG-CLARK, G. T., DRAKE, J. F., REYNOLDS, C. S. & SWISDAK, M. 2018 Suppression of electron thermal conduction by whistler turbulence in a sustained thermal gradient. *Phys. Rev. Lett.* **120**, 035101.

ROSIN, M. S., SCHEKOCHIHIHIN, A. A., RINCON, F. & COWLEY, S. C. 2011 A non-linear theory of the parallel firehose and gyrothermal instabilities in a weakly collisional plasma. *Monthly Notices of the Royal Astronomical Society* **413** (1), 7–38.

SCHEKOCHIHIHIN, ALEXANDER A., COWLEY, STEVEN C., TAYLOR, SAMUEL F., MARON, JASON L. & MCWILLIAMS, JAMES C. 2004 Simulations of the small-scale turbulent dynamo. *The Astrophysical Journal* **612** (1), 276.

SCHOEFFLER, K. M., LOUREIRO, N. F., FONSECA, R. A. & SILVA, L. O. 2014 Magnetic-field generation and amplification in an expanding plasma. *Phys. Rev. Lett.* **112**, 175001.

SCHUBERT, G. & SODERLUND, K.M. 2011 Planetary magnetic fields: Observations and models. *Physics of the Earth and Planetary Interiors* **187** (3), 92–108, special Issue: Planetary Magnetism, Dynamo and Dynamics.

SIRONI, LORENZO, COMISSO, LUCA & GOLANT, RYAN 2023 Generation of near-equipartition magnetic fields in turbulent collisionless plasmas. *Phys. Rev. Lett.* **131**, 055201.

SIRONI, LORENZO, UZDENSKY, DMITRI A. & GIANNIOU, DIMITRIOS 2025 Relativistic magnetic reconnection in astrophysical plasmas: A powerful mechanism of nonthermal emission. *Annual Review of Astronomy and Astrophysics* **63** (Volume 63, 2025), 127–178.

SPITKOVSKY, ANATOLY 2007 On the structure of relativistic collisionless shocks in electron-ion plasmas. *The Astrophysical Journal* **673** (1), L39.

ST-ONGE, DENIS A. & KUNZ, MATTHEW W. 2018 Fluctuation dynamo in a collisionless, weakly magnetized plasma. *The Astrophysical Journal Letters* **863** (2), L25.

SUBRAMANIAN, KANDASWAMY 2016 The origin, evolution and signatures of primordial magnetic fields. *Reports on Progress in Physics* **79** (7), 076901.

SUBRAMANIAN, K., NARASIMHA, D. & CHITRE, S. M. 1994 Thermal generation of cosmological seed magnetic fields in ionization fronts. *Monthly Notices of the Royal Astronomical Society* **271** (1), L15–L18, arXiv: <https://academic.oup.com/mnras/article-pdf/271/1/L15/4002691/mnras271-0L15.pdf>.

TOBIAS, S. M. 2021 The turbulent dynamo. *Journal of Fluid Mechanics* **912**, P1.

VAZZA, F., BRUNETTI, G., BRÜGGEN, M. & BONAFEDE, A. 2017 Resolved magnetic dynamo action in the simulated intracluster medium. *Monthly Notices of the Royal Astronomical Society* **474** (2), 1672–1687, arXiv: <https://academic.oup.com/mnras/article-pdf/474/2/1672/22473785/stx2830.pdf>.

WALTERS, JADA, KLEIN, KRISTOPHER G., LICHKO, EMILY, JUNO, JAMES & TENBARGE, JASON M. 2024 Electron influence on the parallel proton firehose instability in 10-moment, multifluid simulations. *The Astrophysical Journal* **975** (2), 290.

WANG, LIANG, HAKIM, AMMAR H., BHATTACHARJEE, A. & GERMASCHEWSKI, K. 2015 Comparison of multi-fluid moment models with particle-in-cell simulations of collisionless magnetic reconnection. *Physics of Plasmas* **22** (1), 012108.

WANG, LIANG, HAKIM, AMMAR H., NG, JONATHAN, DONG, CHUANFEI & GERMASCHEWSKI, KAI 2020 Exact and locally implicit source term solvers for multifluid-maxwell systems. *Journal of Computational Physics* **415**, 109510.

WEIBEL, ERICH S. 1959 Spontaneously growing transverse waves in a plasma due to an anisotropic velocity distribution. *Phys. Rev. Lett.* **2**, 83–84.

ZHOU, MUNI, ZHDANKIN, VLADIMIR, KUNZ, MATTHEW W., LOUREIRO, NUNO F. & UZDENSKY, DMITRI A. 2022 Spontaneous magnetization of collisionless plasma. *Proceedings of the National Academy of Sciences* **119** (19), e2119831119, arXiv: <https://www.pnas.org/doi/pdf/10.1073/pnas.2119831119>.

ZHOU, MUNI, ZHDANKIN, VLADIMIR, KUNZ, MATTHEW W., LOUREIRO, NUNO F. & UZDENSKY, DMITRI A. 2023 Magnetogenesis in a collisionless plasma: From weibel instability to turbulent dynamo. *The Astrophysical Journal* **960** (1), 12.

ZHURAVLEVA, I., CHURAZOV, E., SCHEKOCHIHIHIN, A. A., ALLEN, S. W., VIKHLLIN, A. & WERNER, N. 2019 Suppressed effective viscosity in the bulk intergalactic plasma. *Nature Astronomy* **3** (9), 832–837.